Accademic year 22-23

Spacecraft attitude dynamics and control project

ADCS performance analysis on a large satellite

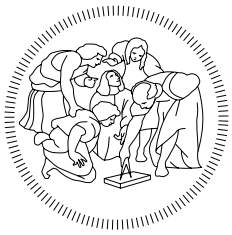

POLITECNICO
MILANO 1863

DIPARTIMENTO DI
SCIENZE E TECNOLOGIE AEROSPAZIALI

Authors: Cambielli Alessandro (10619322): Aerospace Engineering PoliMI

Professor: Franco Bernelli Zazzera

Group ID: 20

	Assigned specification	Modifications	Motivation
Platform	Large spacecraft	-	-
Attitude parameters	DCM	-	-
Sensor	Earth horizon sensor	Magnetometer and gyroscope added	To perform better attitude determination
Actuators	3 magnetic coils and 1 reaction wheel	3 reaction wheels have been added	Explained in the report

Index

1 Introduction

The aim of this report is to investigate the attitude determination and control of a large spacecraft on a LEO orbit. The following report presents the modeling of the dynamics of the spacecraft, the design of the ADCS system and finally the results of numerical simulations. The simulation takes into account the most prominent disturbance torques typical of this environment as well as the performances of the selected ADCS components.
The considered mission profile will be divided in three phases:

1. An uncontrolled phase, right after orbit insertion
2. A de-tumbling phase
3. A tracking phase, which comprehends a slew manoeuvre and an Earth pointing phase

2 Descriprion of the system

2.1 Spacecraft's characteristics and configuration

The assigned project specification demands a spacecraft with a mass higher than 500 Kg. Between a large variety of possibilities, a S/C with a central parallelepiped shaped body, two rectangular solar arrays attached to two opposite faces and an overall symmetric structure has been chosen. The principal axis frame $\{x', y', z'\}$ is coincident with the body frame $\{x, y, z\}$ due to the symmetry of the structure, thus making $r_{CG} = \{0, 0, 0\}\, cm$ in the principal axis frame. The complete specification of the S/C are presented in 1.

$$I = \begin{bmatrix} 785 & 0 & 0 \\ 0 & 447 & 0 \\ 0 & 0 & 782 \end{bmatrix} kgm^2$$

Table 1: Mass and dimensions of the spacecraft

Dimensions	[m]	**Mass**	[Kg]
Main Bus	$1.5 \times 1.8 \times 1.4$	Main Bus (dry/total)	600/1186
Solar Arrays (2x)	$3.2 \times 1.78 \times 0.1$	Solar Arrays	18.4 (2x)

2.2 Sensors

The spacecraft is equipped with a Earth horizon sensor, a magnetometer and a gyroscope. The first one is used to generate measurements of the directions of the Earth with respect to the spacecraft, the second is sensible to Earth's magnetic field, and the last one provides measurements of the angular velocity of the satellite.

2.2.1 Earth horizon sensor

The horizon sensor selected is the dual conical scanning *STD-16*[1] sensor, produced by *Sodern*. Its specifications are reported in table 2.

Table 2: STD-16 specifications

Dimensions	**Mass**	**Average power**	**Output data rate**	**Accuracy**
175 x 208 x 386 mm	3.5 Kg	7.5 W	1 Hz	$< 0.05°$

The sensor frame is aligned with the principal axes, so the rotation matrix from the body frame to the sensor frame $A^{SS}_{s/b}$ is simply the identity matrix $\mathbb{I}_3$.

2.2.2 Magnetometer

The specifications of the selected magnetometer, *DTFM100S* [2] by *Billingley Aerospace & defense*, are presented in table 3. The sensor provides tri-axial measurements of the magnetic field.

Table 3: DTFM100S specifications

Dimensions	**Mass**	**Max. update rate**	**Noise density @ 1 Hz**	**Orthogonality**
82.6 x 35.1 x 32.3 mm	0.1 kg	18 Hz	15 nT	$< 0.1°$

2.2.3 Gyroscope

The *STIM300* [3] inertial measurement unit by *Safran* has been chosen as gyroscope: its characteristcs are reported in table 4.

Table 4: STIM300 specifications

Volume	**Mass**	**ARW**	**RRW**
$< 35cm^3$	$< 55g$	$15\ °/\sqrt{h}$	$< 0.05°/h$

2.3 Actuators

The spacecraft is equipped with a magnetorquer and a reaction wheel.

2.3.1 Magnetorquer

The chosen magnetorquer is the *MT400-2-L* [4], developed by *ZARM Technik AG*. It is composed of three coils which generate magnetic dipoles in three orthogonal directions (which are, in this case, coincident with the axes of the body frame). Its properties are reported in table 5.

Table 5: MT400-2-L specifications

Dimensions	**Mass**	**Max. dipole strength**	**Linear voltage**
952 (len) x 41 (dia) mm	7.8 kg	400 Am^2	18.5 V

2.3.2 Reaction wheel

The selected reaction wheel is the *RW6000* [5] by *Astrofein*. The specifications of this product are reported in table 6.

Table 6: RW6000 specifications

Dimensions	**Mass**	**Inertia moment**	**Max. torque**	**Max. momentum**
460 x 460 x 150 mm	12 kg	$2.274 \cdot 10^{-1}\, kgm^2$	0.2 Nm	100 Nms

3 Description of the model

3.1 Orbit dynamics

Due to the project specification constraints which required the use of an horizon sensor and magnetorquers the orbit chosen is a LEO to maximize the sensors' precision and utility. Between all the possible LEO orbits one with $r_p = 800\,km$ was chosen since it represents the perfect balance between an orbit close enough to Earth to have both precise pointing and ADCS as well as far enough from Earth to limit the gravity gradient disturbance that, due to the S/C's mass would have a high magnitude. The orbit's characteristics are summarized in table 7:

Table 7: Keplerian elements of the orbit

a [km]	e [-]	i [°]	Ω [°]	ω [°]	T[s]
8152	0.1195	21.8583	0	0	7325

The time law for elliptical orbits shown in eq. (1) is used to compute the orbit propagation:

$$\dot{\theta} = \frac{n(1 + e\cos(\theta))^2}{(1 - e^2)^{\frac{2}{3}}} \tag{1}$$

where $n = 1/T$ is the mean orbital motion. The integration of the true anomaly allows for the computation of the position and the velocity of the spacecraft in the Earth Centered Inertial (ECI) frame (respectively $\mathbf{r}_{S/C}$ and $\mathbf{v}_{S/C}$) at any time. The orbit is shown in fig. 1.

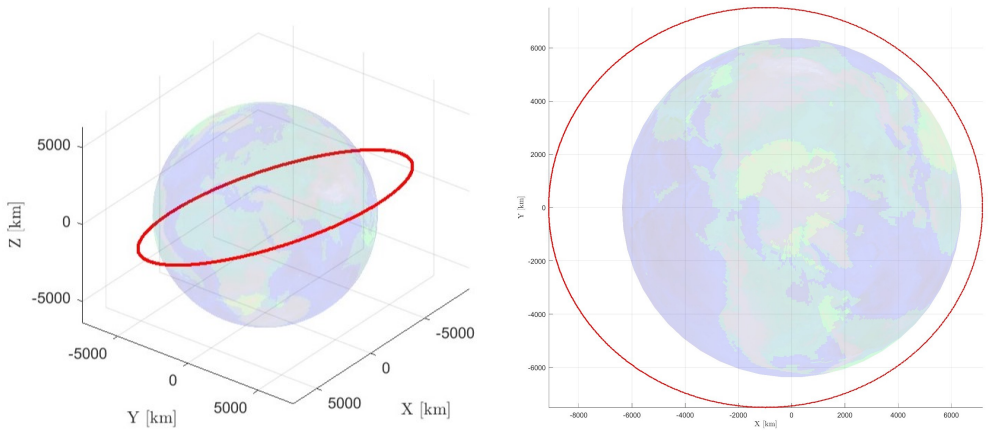

(a) Orbit plot

(b) Orbit on X-Y plane

Figure 1: Selected Low Earth Orbit

3.2 Dynamics and kinematics

Modelling the spacecraft as a rigid body, the dynamics is derived from the integration of the Euler's equations:

$$I\frac{d\boldsymbol{\omega}}{dt} = I\boldsymbol{\omega} \times \boldsymbol{\omega} + \mathbf{M_c} + \mathbf{M_d} \tag{2}$$

Where $\boldsymbol{\omega} = [\omega_x, \omega_y, \omega_z]^T$ is the angular velocity of the satellite, $\mathbf{M_c}$ is the control torque, and $\mathbf{M_d}$ is the disturbing torque, all expressed in the body reference frame.
The numerical integration of eq. (2) returns the value of the angular velocity, which can subsequently be used to propagate the attitude kinematics of the satellite.
The assigned attitude parameter, which describes the orientation of the body frame with respect to the inertial frame, is the direction cosine matrix: it describes the rotation from one reference frame to another. Each element of the matrix represents the rotational variations that, applied on any vector in the first reference frame, gives the same vector expressed in the second reference frame.
The kinematics describe the variation in time of the DCM, according to eq. (3) and eq. (4).

$$\frac{dA}{dt} = \lim_{\Delta t \to 0} \frac{A(t+\Delta t) - A(t)}{\Delta t} = \lim_{\Delta t \to 0} \frac{\Delta t[\omega\,\Lambda]A(t)}{\Delta t} = -[\omega\,\Lambda]A(t) \tag{3}$$

Where:

$$[\omega\,\Lambda] = \begin{bmatrix} 0 & -\omega_z & \omega_y \\ \omega_z & 0 & -\omega_1 \\ -\omega_y & \omega_1 & 0 \end{bmatrix} \tag{4}$$

Given the angular velocity and the initial condition for the DCM, equation 3 can be numerically integrated, obtaining the attitude of the considered object.
In order to be consistent with the physics of the problem, the DCM has to be normalized in order to preserve its property of having unitary magnitude. For this reason a first order orthonormalization is performed at every time step:

$$A(t) = \frac{3}{2}A_0(t) - \frac{1}{2}A_0(t)A_0^T(t)A_0(t) \tag{5}$$

Where $A(t)$ is the orthonormalized matrix, and A_0 is the solution of numerical integration.

3.3 External disturbances

The total disturbance torque M is made up of three contributions: M_b from the interaction with the magnetic field, M_{GG} from the gravity gradient and M_{SRP} from solar radiation pressure.

3.3.1 Magnetic disturbance

The magnetic field acting on the spacecraft could generate a relevant disturbance to the dynamics of a S/C depending on its mission. An analysis of the disturbance torque produced is needed to verify its magnitude relative to the other disturbances.
The magnetic torque is given by eq. (6):

$$\mathbf{M}_b = \mathbf{m} \times \mathbf{B}_b = \mathbf{m} \times (A_{B/N}\mathbf{B}_n) \tag{6}$$

$$\mathbf{m} = [0.1;\ 0.1;\ 0.1]\ Am^2 \tag{7}$$

Where $\mathbf{m}$ is is the parasitic magnetic moment of the spacecraft, eq.7, and $\mathbf{B}_b$ is the magnetic field in the body frame.
In order to achieve the maximum precision possible the magnetic field is designed using the **IGRF** model (International Geomagnetic Reference Field), that describes the magnetic field in the inertial frame until the 13th term of expansion[6].
This model is implemented on a Matlab function that numerically integrates the problem's equations and returns the coefficients of the field B, up to the 13^{th} degree of precision. Regarding the dipole moment m, the selected vector represents an average value for a spinning S/C as explained in [7].

3.3.2 Gravity gradient

The torque caused by the gravity gradient is computed as shown in eq. (8):

$$\mathbf{M}_{GG} = \frac{3\mu_E}{\|\mathbf{r}_{S/C}\|^3} \begin{Bmatrix} (I_z - I_y)\, c_2\, c_3 \\ (I_x - I_z)\, c_1\, c_3 \\ (I_y - I_x)\, c_1\, c_2 \end{Bmatrix} \tag{8}$$

Equation 8 holds as long as the inertia matrix I is a diagonal matrix.
The terms c_1, c_2, c_3 are computed according to Equation 9:

$$\begin{bmatrix} c_1 \\ c_2 \\ c_3 \end{bmatrix} = A_{L/N} A_{B/N}^T \begin{bmatrix} 1 \\ 0 \\ 0 \end{bmatrix} = A_{B/L} \begin{bmatrix} 1 \\ 0 \\ 0 \end{bmatrix} \tag{9}$$

The gravity gradient's magnitude is the highest between all the environment disturbances which is justified by the LEO orbit of the S/C and by the high inertia values which are a consequence to the S/C's dimensions.

3.3.3 Solar radiation pressure

The solar radiation force acting on the S/C is computed using the following eq. (10):

$$\mathbf{F_i} = -PA_i(\hat{S}_B \cdot \hat{N}_{Bi}) \left[(1-\rho_S)\hat{S}_B + (2\rho_S(\hat{S}_B \cdot \hat{N}_{Bi}) + \frac{2}{3}\rho_D)\hat{N}_{Bi} \right] \tag{10}$$

where $\hat{N}_{Bi}$ are the normal to each face of the spacecraft, which are 6 versors for the main body and 4 for the solar panels (2 for each solar panel since it is a low thickness body), S_B is the Sun's direction expressed in body frame, P is the average pressure due to radiation, ρ_S is the coefficient of specular reflection, ρ_D is the coefficient of diffuse reflection.
Considering each axis of the body, since only one side of each axis plane is illuminated the simulation computes the dot product $\hat{S}_B \cdot \hat{N}_{Bi}$ and creates a pointer vector to store the information of which side is illuminated.
The forces are then computed for both the main body and the solar panels in matrix form in which each column corresponds to each axis plane illuminated (3 for the main body and 1 for the solar panel) in the order $\pm x$, $\pm y$, $\pm z$ (where the sign is the same as the pointer defined before).
The arm of the force to compute the torque is then evaluated using the distance between the centre of mass of the whole S/C (which coincides with the geometrical centre since it is symmetrical) and the centre of pressure of the solar radiation force distribution on the S/C's faces.
The center of pressure is computed using the area projection of each face in the direction of the Sun and it is possible to verify that there is a small shift of this point from the geometrical centre of the illuminated faces which generates a small net torque on the S/C even if it is symmetrical.

3.4 Sensors

The behaviour of the **Earth horizon sensor** hasn't been simulated, instead the measurements made by the sensor is modeled by taking into account uncertainties through a linearized error ro-

tation matrix $A_{123}(\phi, \theta, \psi)$. The terms ϕ, θ, ψ are randomly generated Euler angles from a Gaussian distribution with zero mean value and standard deviation equal to the accuracy of the sensor reported in table 2. The measurement vectors have been computed as:

$$\mathbf{v}_{B_i} = A_{err}\, A_{B/N}\, \mathbf{v}_{N_i} \tag{11}$$

where A_{err} is the error matrix related to the sensors, while $\mathbf{v_{B_i}}$ and $\mathbf{v_{N_i}}$ are the measurements vectors respectively in body and inertial frame. The considered measurements are the position vectors of the satellite $\mathbf{r}$.

A **gyroscope** is simulated to retrieve the measurements of angular velocities. A simple solid-state gyro noise model has been implemented to obtain a noisy measurement of the angular velocities of the form:

$$\omega_i^m = \omega_i + \sigma_n \zeta_n + \sigma_b \zeta_b \tag{12}$$

The two additive terms are white Gaussian noises with zero mean and standard deviations of the form σ_i, respectively dependent on the angular random walk (ARW) and the rate random walk (RRW).

Magnetometers provide the measurement of the direction of the magnetic field in the body frame. They do require a well-modelled magnetic field if they are to be used as attitude sensors. The measurements of the magnetometer are modeled considering two types of error: a bias on the three components of the magnetic field and an error due to the non-orthogonality of the axes of the sensor. The first error is a vector $\boldsymbol{\epsilon}$ in which each component is assumed to be constant (table 3). The non-orthogonality of the axis is introduced through a linearized rotation error matrix $A_{123}(\phi, \theta, \psi)$, where the angles are taken from Gaussian distributions with zero mean value and standard deviation equal to the orthogonality accuracy of the sensor reported in talbe 3. Therefore the measured magnetic field in body frame is the hereon shown in eq. 13:

$$\tilde{\mathbf{b}}_b = A_{err}\,(\phi, \theta, \psi)\,(\mathbf{b}_b + \boldsymbol{\epsilon}) \tag{13}$$

3.5 Actuators

The **magnetorquer** can generate a torque based on its magnetic dipole vector $\mathbf{D}$, which is the variable in the control design.

$$\mathbf{M}_{MT} = \mathbf{D} \times \mathbf{b}_b \tag{14}$$

The magnetorquer selected for the assigned spacecraft is able to guarantee a high linear dipole moment, and consequently more controllability. It is mounted along the three principal axis of the s/c. The absolute values of the three components of the dipole must not exceed the values reported in table 5, thus $|D_i| < D_{i,max}$.

The **reaction wheels** are momentum exchange devices, so they shall be included in the total angular momentum of the system. The single reaction wheel has been placed along the x-axis after a trial-and-error approach to find the better positioning. The control torque provided by the actuator is computed as:

$$\mathbf{M}_{RW} = -\hat{\mathbf{a}}_{RW}\dot{h}_r - \boldsymbol{\omega} \times h_r \hat{\mathbf{a}}_{RW} \tag{15}$$

Where the dynamic of the wheels can be propagated as:

$$\dot{h}_r = (-\mathbf{M}_{RW} - \boldsymbol{\omega} \times \hat{\mathbf{a}}_{RW} h_r) \cdot \hat{\mathbf{a}}_{RW} \tag{16}$$

To compare different detumbling scenarios, three other identical components have been added to the actuation system. Considering the internal dynamics of the wheels and no other actuator, the set of equations describing the rotational dynamics of the spacecraft becomes:

$$\begin{cases} \mathbf{h} = I\boldsymbol{\omega} + A\mathbf{h}_r & \text{(17a)} \\ I\boldsymbol{\omega} + \boldsymbol{\omega} \times I\boldsymbol{\omega} + A\dot{\mathbf{h}}_r + \boldsymbol{\omega} \times A\dot{\mathbf{h}}_r = \mathbf{M}_d & \text{(17b)} \\ I_r\dot{\mathbf{h}}_r = \mathbf{M}_r & \text{(17c)} \end{cases}$$

A is a matrix composed by three rows and four columns (as the number of actuators). For the pyramid configuration, A and its pseudo-inverse A^* are shown in eq. 18:

$$A = \frac{1}{\sqrt{3}} \begin{bmatrix} -1 & 1 & 1 & -1 \\ -1 & -1 & 1 & 1 \\ 1 & 1 & 1 & 1 \end{bmatrix}, \quad A^* = \frac{\sqrt{3}}{4} \begin{bmatrix} -1 & -1 & 1 \\ 1 & -1 & 1 \\ 1 & 1 & 1 \\ -1 & 1 & 1 \end{bmatrix} \tag{18}$$

Each column of A represents the direction of the axis of rotation of the i-th wheel, having angular momentum equal to $h_{r,i}$. These last values are gathered in the vector $\mathbf{h}_r$, which has therefore four components. The scalar I_r represents the moment of inertia of the single wheels. The vector $\mathbf{M}_r$ has four components and measures the torque applied to each wheel to make them spin. The actual torque delivered by the actuator to the spacecraft will therefore be according to eq. 19.

$$\mathbf{M}_{RW} = -A\dot{\mathbf{h}}_r - \boldsymbol{\omega} \times A\mathbf{h}_r \tag{19}$$

$\mathbf{M}_{RW}$ is the target of the control design for this actuator. The dynamics of the wheels can subsequently be propagated through the following differential eq. 20:

$$\dot{\mathbf{h}}_r = -A^*[\mathbf{M}_{RW} + \boldsymbol{\omega} \times A\mathbf{h}_r] \tag{20}$$

As the spacecraft is not equipped with any de-saturation mechanism, it must be always verified that $|\mathbf{M}_r| < \mathbf{M}_{r,max}$ and $|\mathbf{h}_r| < \mathbf{h}_{r,max}$. The values for $\mathbf{M}_{r,max}$ and $\mathbf{h}_{r,max}$ are reported in table 6.

4 Attitude Determination

The attitude determination is the computation of the attitude parameters starting from the available measurements, retrieved by the sensors. The attitude determination adopted is based on the analytic solution of the Wabha's problem. This problem consists in the minimization of the following weighted function:

$$J = \frac{1}{2}\sum_{k=1}^{N} \alpha_i \left|\mathbf{s}_{Bi} - A_{B/N}\mathbf{v}_{Ni}\right|^2 \tag{21}$$

In which N is the number of attitude sensors, α_i are normalized constants related to the sensor precision, $\mathbf{s}_{Bi}$ are the measurements vectors in body frame and $\mathbf{v}_{Ni}$ are the vectors of the real quantities in the inertial frame. The optimal solution to the Wabha's problem is the one one that maximises the function: $\tilde{J} = tr\left(A_{B/N}B^T\right)$.
$A_{B/N}$ can be retrieved by single value decomposition (SVD) of matrix B, where $B = \sum_{k=1}^{N} \alpha_i s_{Bi} v_{Ni}^T$, exploting the following relationships:

$$B = USV^T \tag{22}$$

$$M = diag\left(1,\ 1,\ detU\, detV\right) \tag{23}$$

$$A_{B/N} = UMV^T \tag{24}$$

The measurements involved in our computation are those obtained from the horizon sensor and the magnetic sensor. The contributes in the function $f(J)$ are weighted using the normalized accuracy of the modelled sensor.

4.1 Extended State Observer (ESO)

The Extended State Observer (*ESO*) is implemented in order to further filter out the estimation of the angular velocity $\bar{\omega}$ and to estimate the unknown disturbances acting on the satellite: the model is described in eq. (25).

$$\begin{cases} \dot{\bar{\boldsymbol{\omega}}} = I^{-1}\left(I\bar{\boldsymbol{\omega}} \times \bar{\boldsymbol{\omega}} + \bar{\mathbf{M}}_c + \bar{\mathbf{M}}_d\right) + L_\omega\left(\boldsymbol{\omega}_m - \bar{\boldsymbol{\omega}}\right) & \text{(25a)} \\ \dot{\bar{\mathbf{M}}}_d = L_d\left(\boldsymbol{\omega}_m - \bar{\boldsymbol{\omega}}\right) & \text{(25b)} \end{cases}$$

$\bar{\mathbf{M}}_\mathbf{c}$ is the estimated control torque, which can be computed once that the control logic is defined through measured and estimated quantities. The gains are set equal to $L_w = 0.8$ and $L_d = 1 \cdot 10^{-5}$ after trial-and-error iterations. The term $\bar{\mathbf{M}}_d$ will be used in the design of the control laws as it can increase the robustness and the disturbance rejection capabilities of the control system.

5 Mission overview

As already stated in section 1, the mission profile considered for the design of the control logic and for the following simulations is split into three phases:

1. **uncontrolled**: in this phase the spacecraft is not controlled, as it is assumed that the ADCS system is not fully operational yet. The simulation is useful to analyze the disturbances acting on the satellite.

2. **detumbling**: the aim of this phase is to reduce the angular velocity of the satellite as close to zero as possible.

3. **tracking**: in this phase, the goal is to constantly point the payload of the satellite towards the centre of the Earth. This condition is verified when the x-axis of the satellite body frame is aligned with the 1^{st} axis of the LVLH frame, which is parallel to the orbit radial direction. The performance parameter which describes the precision in the tracking is the pointing error, defined as the angle between the two directions ar reported in eq. 26.

$$p = \arccos\left(\hat{\mathbf{x}}_b^T\, \hat{\mathbf{x}}_l\right) = \arccos\left(\begin{bmatrix} 1 & 0 & 0 \end{bmatrix} A_{B/N}\, A_{L/N}^T \begin{bmatrix} 1 \\ 0 \\ 0 \end{bmatrix}\right) = \arccos\left(A_{B/L\ 1,1}\right) \qquad (26)$$

For mission purposes, the pointing error shall be maintained below $1°$.

5.1 Detumbling control

The detumbling phase is simulated both for a single and a set of 4 reaction wheels and two different control strategies are consecutively implemented:

1. a **spin rate damping** (*SRD*) control law, in which only the magnetorquer is employed.
2. a **proportional** control law using the reaction wheels.

The first control strategy is expected to last $5000\,s$ ($1.39\,h$, ≈ 0.68 orbital periods) when combined with 4 reaction wheels, and $20000\,s$ ($5.55\,h$, $\approx$ 2.73 orbital periods) when combined with just a single reaction wheel, and is exploited to avoid an early saturation of the reation wheels. The second control technique is simulated until $70000\,s$ ($19.44\,h$, ≈ 9.55 orbital periods) and is expected to detumble completely the spacecraft in both cases. The high detumbling time is due to the high mass of the spacecraft and the intrinsic low torque provision capacity of the actuators, but it appears reasonable considering the longevity of the mission (dozens of years of activity). For the **first control strategy**, the analytical expression of the ideal control dipole is $\mathbf{D}^{id} = -k_b\,\dot{\mathbf{b}}_b$. Assuming that the time variations are only due to the rotation of the satellite, the derivative of the magnetic field in the body frame is approximated as $\dot{\mathbf{b}}_b \approx -\boldsymbol{\omega} \times \mathbf{b}_b$. Considering that the magnetorquer relies on measurements and estimations coming from the attitude determination system, the ideal commanded dipole would be $\mathbf{D}^{id} = k_b\,\bar{\boldsymbol{\omega}} \times \tilde{\mathbf{b}}_b$. The ideal control moment that the magnetorquer should provide is:

$$\mathbf{M}_c^{id} = k_b\,(\bar{\boldsymbol{\omega}} \times \tilde{\mathbf{b}}_b) \times \bar{\mathbf{b}}_b - \bar{\mathbf{M}}_d \text{ with } k_b = 10^9 \tag{27}$$

The term $\bar{\mathbf{M}}_d$ is added for robustness, as reported in section 4.1. As the control moment can only be perpendicular to the magnetic field, a possible strategy is to generate a real dipole (depending on the $\mathbf{M}_c^{id}$) always normal to $\mathbf{b}_b$. This would be theoretically possible with the exact knowledge of the magnetic field, in this case retrieved from the magnetometer measurements. The expression of the real commanded dipole is then:

$$\bar{\mathbf{D}} = \frac{\tilde{\mathbf{b}}_b \times \mathbf{M}_c^{id}}{\|\tilde{\mathbf{b}}_b\|^2} \tag{28}$$

The effective control torque provided by magnetorquer and its estimation (required for the ESO) will have the following expressions:

$$\mathbf{M}_c = \frac{1}{\|\tilde{\mathbf{b}}_b^2\|}\left(\tilde{\mathbf{b}}_b \times \mathbf{M}_c^{id}\right) \times \mathbf{b}_b, \qquad \bar{\mathbf{M}}_c = \frac{1}{\|\tilde{\mathbf{b}}_b^2\|}\left(\tilde{\mathbf{b}}_b \times \mathbf{M}_c^{id}\right) \times \tilde{\mathbf{b}}_b \tag{29}$$

In the **second control strategy**, the ideal control torque that shall be provided for both cases is:

$$\mathbf{M}_c^{id} = -k_p\bar{\boldsymbol{\omega}} - \bar{\mathbf{M}}_d \qquad \text{with } k_p = 10^{-1} \tag{30}$$

The real torque exerted on the spacecraft $\mathbf{M}_c$ is computed propagating eqs. (15), (16), (19) and (20). The estimation $\bar{\mathbf{M}}_c$ can be derived from the same equations by considering the estimated angular velocity $\bar{\boldsymbol{\omega}}$ instead of the actual one.

5.2 Tracking control

The tracking phase starts right after the end of the detumbling control and has been performed exploiting 4 reaction wheels only, as it needs an high torque capacity. This phase is simulated for $40000\,s$ ($11.11\,h$, ≈ 5.46 orbital periods). The spacecraft performs initially a slew motion in order to re-orient itself in the correct direction and at the correct angular velocity. The control system shall then be able to constantly track the Nadir direction, described by the 1^{st} axis of the LVLH frame. The desired angular velocity and direction cosines matrix are defined then as:

$$\boldsymbol{\omega}_d = \begin{bmatrix} 0 & 0 & \dot{\theta} \end{bmatrix}^T, \qquad A_d = A_{L/N} \tag{31}$$

$\dot{\theta}$ is known from orbital dynamics. The error angular speed and the error DCM are defined as:

$$\boldsymbol{\omega}_e = \bar{\boldsymbol{\omega}} - A_e\,\boldsymbol{\omega}_d, \qquad A_e = \bar{A}_{B/N}\,A_d^T \tag{32}$$

A non-linear control law is implemented and allocated to the reaction wheels through eqs. (19) and (20). It is derived using a Lyapounov function:

$$\mathbf{M}_c^{id} = -k_\omega\boldsymbol{\omega}_e - k_{A_e}[A_e^T - A_e]^V + \bar{\omega} \times I\bar{\omega} - \bar{\mathbf{M}}_d \qquad \text{with: } k_\omega = 0.5,\ k_{A_e} = 0.5 \tag{33}$$

with:

$$[A_e^T - A_e]^V = [A_{e\,2,3} - A_{e\,3,2},\ A_{e\,3,1} - A_{e\,1,3},\ A_{e\,1,2} - A_{e\,2,1}]^T \tag{34}$$

6 Simulation framework

A block diagram of the simulation framework is reported in fig. 2. The graph highlights the interconnections between the various blocks which are used to simulate the dynamics of the spacecraft and of the ADCS system.

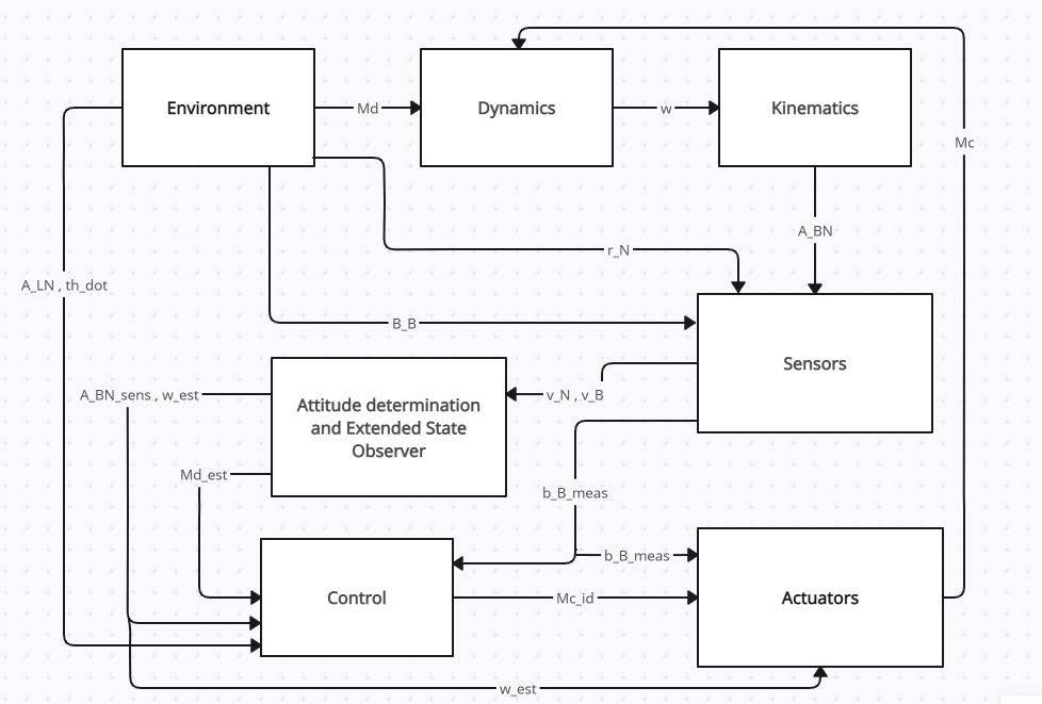

Figure 2: Simulation framework

7 Numerical simulation results

7.1 Uncontrolled dynamics

The uncontrolled dynamics of the satellite is simulated for one orbital period (equal to ≈ 2 hours). The starting time is set to $t_0 = 0\,s$. The initial conditions are the following:

$$\boldsymbol{\omega}_0 = \begin{bmatrix} 3 & 11 & 14 \end{bmatrix}^T \, ^\circ/s, \qquad hr_0 = \begin{bmatrix} 0 & 0 & 0 & 0 \end{bmatrix}^T, \qquad \theta_0 = 30^\circ, \qquad \bar{\mathbf{M}}_{d,0} = \begin{bmatrix} 0 & 0 & 0 \end{bmatrix}^T \, Nm$$

The evolution in time of the disturbing torques, of the angular velocity and of the pointing error are reported in figs. 3 and 4, while table 8 reports the maximum magnitude of the four disturbing torques.

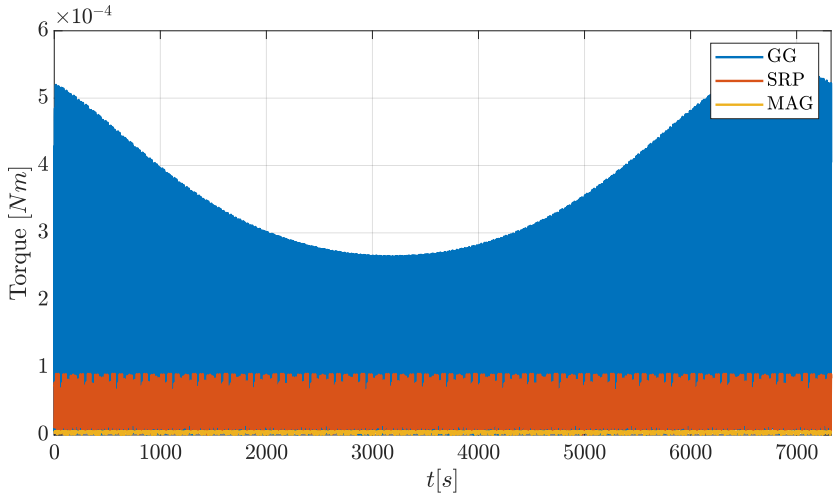

Figure 3: Evolution of GG, MAG, and SRP disturbances acting on the spacecraft

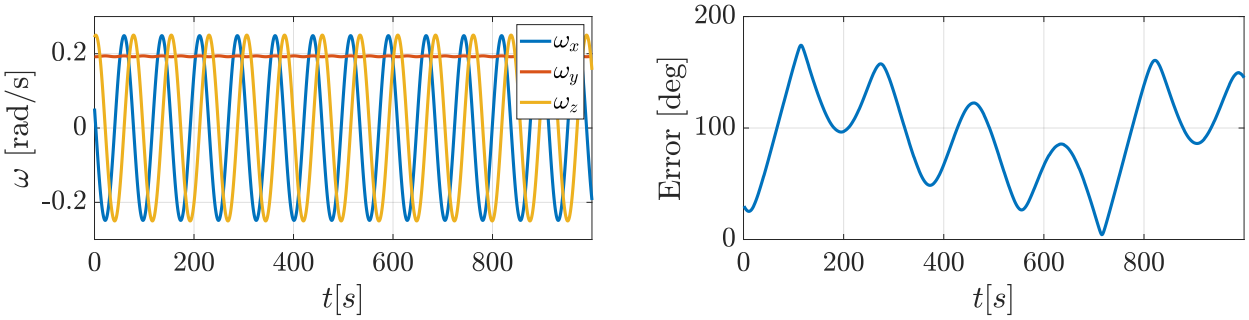

(a) Angular velocity

(b) Pointing error

Figure 4: Evolution of $\boldsymbol{\omega}$ and pointing error in uncontrolled dynamics for a reduced time window

It is clear that the main disturbances are due to the gravity gradient, caused by the satellite's large mass. The other disturbances impact is way lower.

Table 8: Maximum magnitude of the disturbing torques

	$\mathbf{M}_{GG}$	$\mathbf{M}_{MAG}$	$\mathbf{M}_{SRP}$
Max. magnitude $[Nm]$	$5.45 \cdot 10^{-4}$	$5.22 \cdot 10^{-6}$	$9.07 \cdot 10^{-5}$

7.2 Detumbling

The detumbling phase is simulated from $t_0 = 0\,s$ to $t_{end} = 70000\,s\,(19.44\,h)$ for both the control with 1 and 4 reaction wheels combined with a magnetorquer. The initial conditions for this phase are the same specified for the uncontrolled dynamic. The results of the evolution of the angular velocity for the control logics selected are presented in fig. 5.

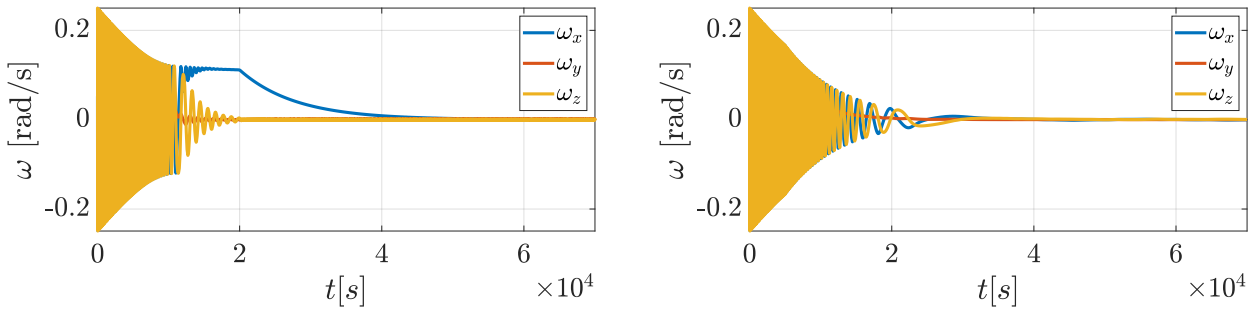

(a) detumbling with 1 reaction wheel

(b) detumbling with 4 reaction wheels

Figure 5: Evolution of $\boldsymbol{\omega}$ in the detumbling phase for both strategies

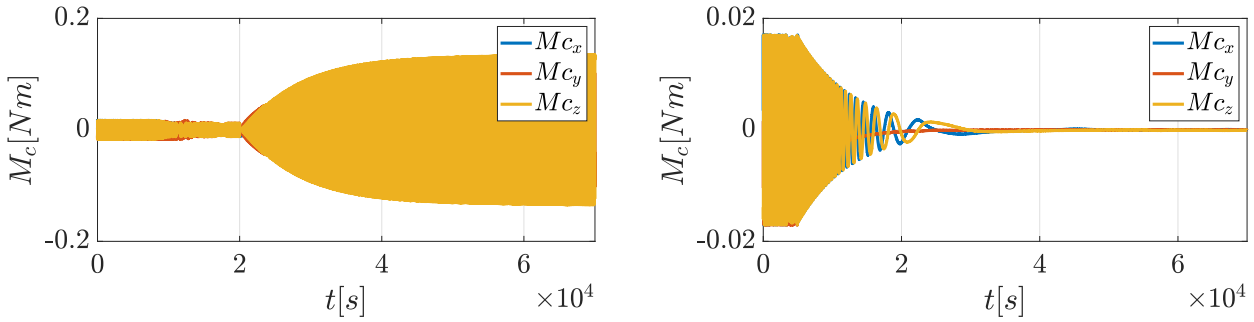

(a) Torque obtained from 1 reaction wheel

(b) Torque obtained from 4 reaction wheel

Figure 6: Evolution of $\boldsymbol{M_c}$ in the detumbling phase for both strategies

Exploiting 4 reaction wheels instead of 1 provides a more efficient detumbling: $\boldsymbol{\omega}$ drops closer to zero and stabilizes itself after $\approx 40000\,s\,(11.11\,h)$. Utilizing just 1 reaction wheel, the detumbling can be considered to be completed in $\approx 60000\,s\,(16.67\,h)$. Especially the ω_x component of the angular velocity faces a slower decay: this is due to the lower available torque along the three axis. The values of the angular velocity at the end of the control phase are reported in table 9.

Table 9: Values of the angular velocity after the detumbling phase

$\boldsymbol{\omega}$ **after the detumbling control** $[rad/s]$	
1 reaction wheel	4 reaction wheels
$\begin{bmatrix}4.86 & 0.32 & -16.0\end{bmatrix}^T \cdot 10^{-4}$	$\begin{bmatrix}-1.23 & 0.83 & -3.63\end{bmatrix}^T \cdot 10^{-4}$

Figure 6 shows that the system with a single reaction wheel is heavily underactuated: it requires a large torque (close to the maximum achievable) even during the final stages of the detumbling phase, when the angular velocity approaches 0. This kind of behaviour makes it unrealistic to achieve a slew manoeuvre, which requires an even higher torque, with this actuation system. On the other hand the system of 4 reaction wheels behaves much better, as the torque is better allocated. During the detumbling phase the attitude determination algorithm is supposed to be still turned off. The attitude determination is then retrieved through the integration of eq. (2) exploiting the measurements of ω obtained from the ESO. The performances of the Extended State Observer are presented through the plots in figs. 7 and 8. The estimations of both $\boldsymbol{\omega}$ and $\mathbf{M_d}$ are considered satisfactory during the whole time window.

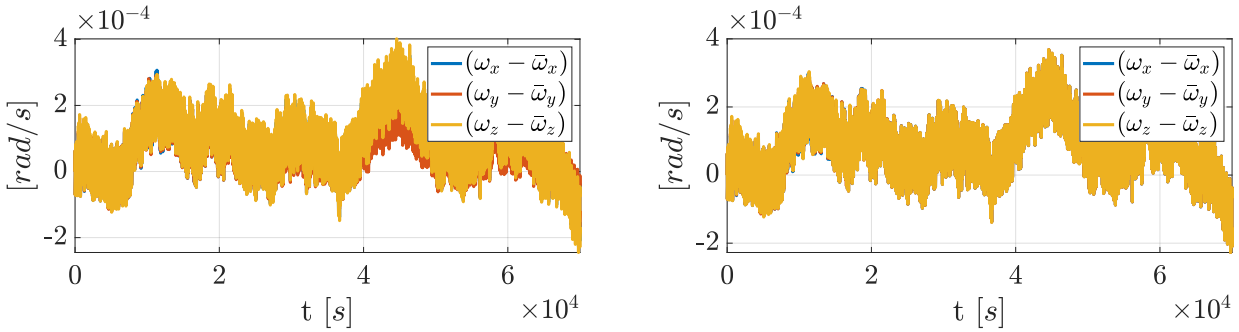

(a) 1 reaction wheel

(b) 4 reaction wheel

Figure 7: Evolution of the estimation error on $\boldsymbol{\omega}$ during the detumbling phase

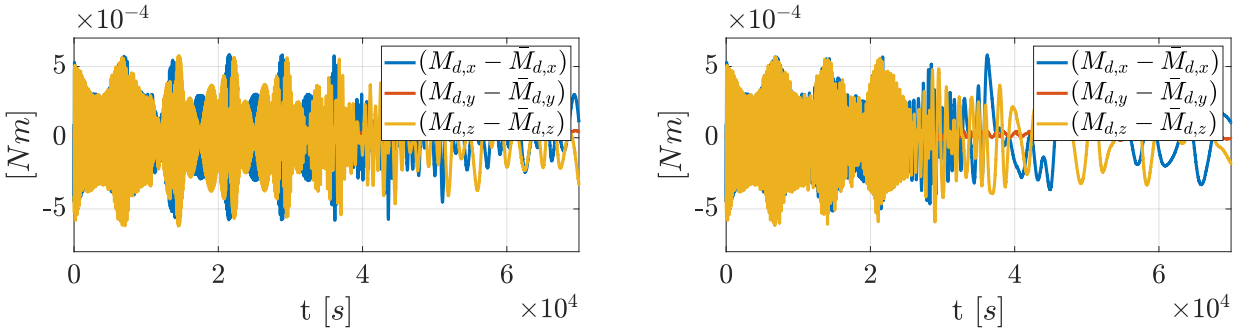

(a) 1 reaction wheel

(b) 4 reaction wheel

Figure 8: Evolution of the estimation error on $\mathbf{M_d}$ during the detumbling phase

7.3 Tracking

The tracking phase is simulated from $t_0 = 70000\,s\,(19.44\,h)$ to $t_{end} = 110000\,s\,(30.55\,h)$. For this phase only the control strategy with 4 reaction wheels has been implemented for the reasons explained in section 7.2. The initial conditions for this simulation are retrieved from the final conditions of the detumbling phase:

$$\boldsymbol{\omega}_0 = \begin{bmatrix} -1.66 & -0.20 & 1.61 \end{bmatrix}^T \cdot 10^{-4}\ rad/s, \qquad \mathbf{h}_{r,0} = \begin{bmatrix} -56.51 & -62.64 & 55.63 & 61.77 \end{bmatrix}^T\ Nms$$

$$A_{B/N_0} = \begin{bmatrix} -0.1664 & 0.9470 & 0.2749 \\ 0.5546 & -0.1406 & 0.8201 \\ 0.8153 & 0.2890 & -0.5018 \end{bmatrix} \tag{35}$$

The results of the simulations are presented in the plots below. The spacecraft is re-oriented in $20000\,s\,(\approx 5.55\,h)$ and after that the Earth pointing phase is simulated for ≈ 3 orbital periods. It is clear from fig. 10 that the control logic fulfills the requirements, as the pointing error is always kept below 1°. The first two components of the angular velocity drop to zero, while the third one oscillates as expected around the orbital mean motion $n = 1/T$, as shown in fig. 9.

For this phase, the performances of the attitude determination and of the ESO are presented through the plots in fig. 11 and fig. 12. The errors associated to the disturbances torque, control torque and angular velocity rapidly drop after an initial transient of $\approx 1000\,s$. A different trend can be observed for the evolution of the attitude matrix, where the error estimated by the attitude determination algorithm remains almost evenly constant except for an isolated integration error at around $87000s$.

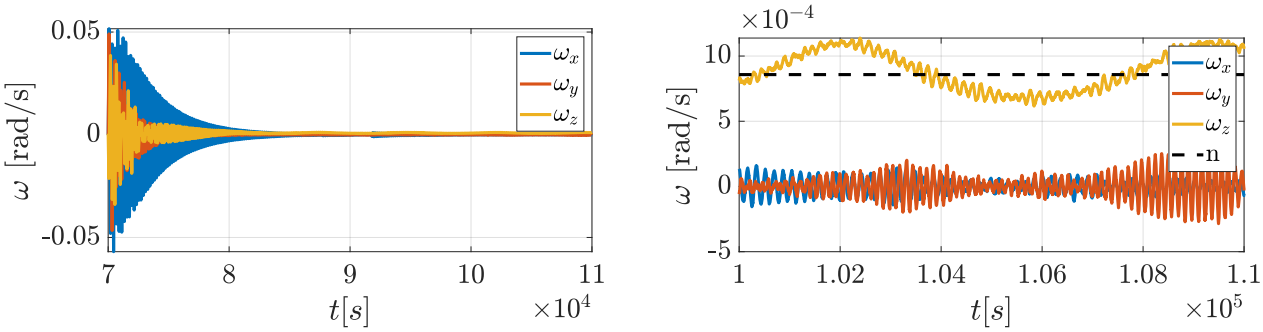

(a) Angular velocity

(b) Angular velocity (detail)

Figure 9: Evolution of $\boldsymbol{\omega}$ in the tracking phase

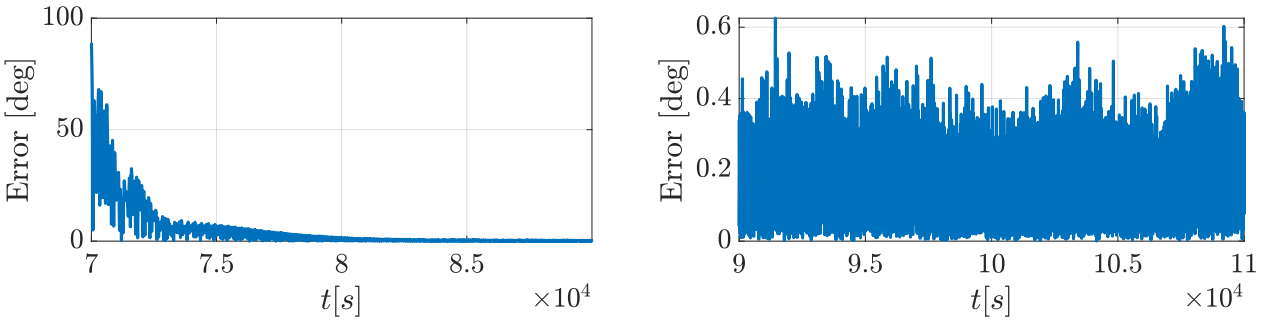

(a) Pointing error during slew manoeuvre

(b) Pointing error during Earth pointing

Figure 10: Evolution of the pointing error in the tracking phase

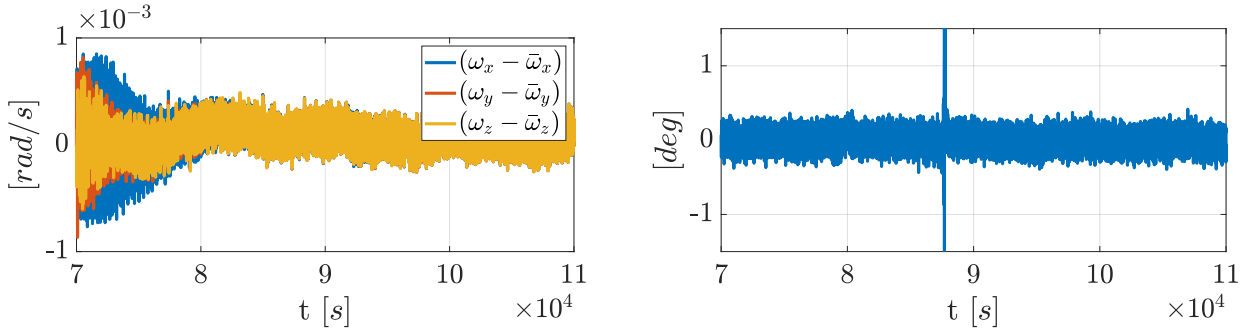

(a) Angular velocity

(b) Attitude matrix error

Figure 11: Evolution of the estimation errors ($\boldsymbol{\omega}$ and A_{BN}) in the tracking phase

The torque provided by the wheels $\mathbf{M}_c$ (fig. 13), initially really high due to the large effort needed for the slew manoeuvre, shows a fast decay as the spacecraft reaches the desired attitude.

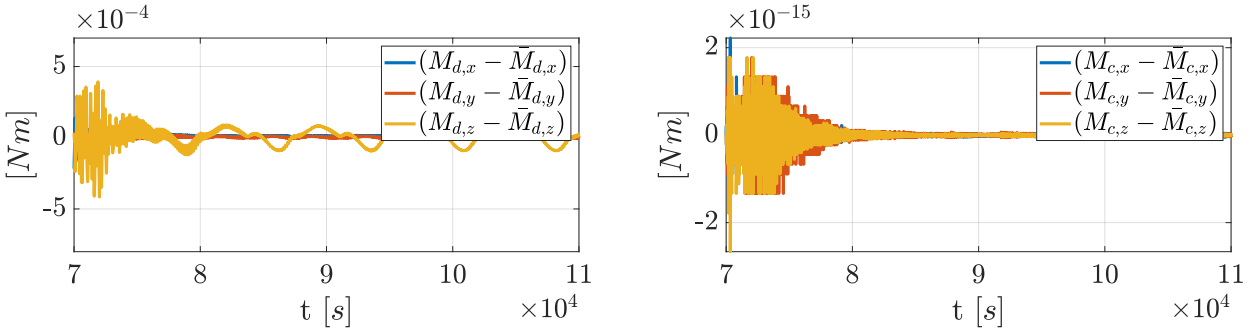

(a) Disturbing torque

(b) Control torque

Figure 12: Evolution of the estimation errors ($\mathbf{M}_d$ and $\mathbf{M}_c$) in the tracking phase

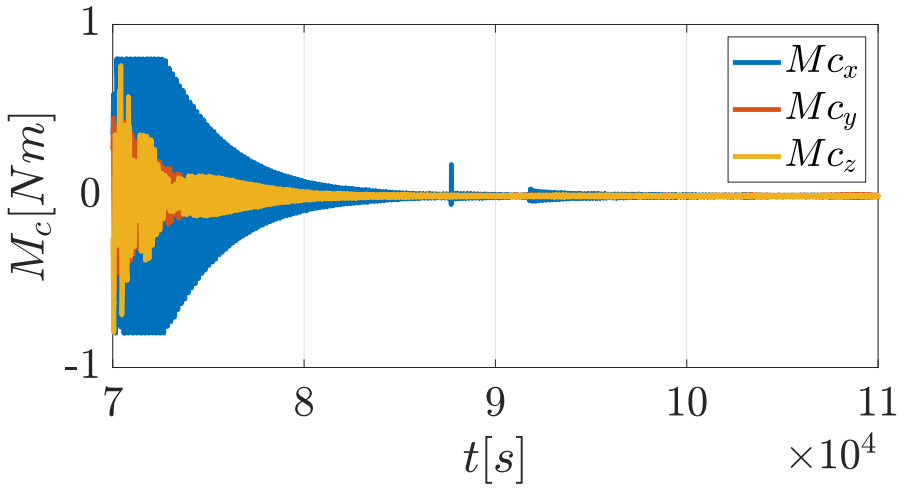

Figure 13: Torque provided by the wheels

8 Conclusions

The performed numerical simulations indicate that the design of the control system is satisfactory and robust. Detumbling is achieved either utilizing 1 or 4 reaction wheels combined with a magnetorquer (though with different degrees of satisfaction and speed). The tracking phase was performed exploiting only 4 reaction wheels, and the pointing error is kept below the required limit with a sufficiently large margin. In order to achieve more realistic results, the model of the system shall be improved implementing some features as including perturbations for the orbital dynamics. In addition the attitude determination and subsequent estimations shall be improved by choosing more precise sensors with faster update rates and by exploiting a different observer.

References

[1] Sodern. *STD-16 horizon sensor datasheet*. URL: https://satcatalog.s3.amazonaws.com/components/14/SatCatalog_-_Sodern_-_STD_16_-_Datasheet.pdf?lastmod=20210708013816.

[2] Billingley Aerospace & defense. *DTFM100S magnetometer datasheet*. URL: https://satcatalog.s3.amazonaws.com/components/102/SatCatalog_-_Billingsley_Aerospace__Defense_-_DTFM100S_-_Datasheet.pdf?lastmod=20210708023812.

[3] Safran. *STIM 300 gyroscope datasheet*. URL: https://www.sensonor.com/products/inertial-measurement-units/stim300/.

[4] ZARM Technik AG. *MT400-2-L magnetorquers datasheet*. URL: https://satcatalog.s3.amazonaws.com/components/139/SatCatalog_-_ZARM_Technik_AG_-_MT400-2-L_-_Datasheet.pdf?lastmod=20210708025605.

[5] Astrofein. *RW6000 reaction wheel datasheet*. URL: https://www.astrofein.com/en/reaction-wheels/rw6000/.

[6] Jeremy Davis. *Mathematical Modeling of Earth's Magnetic Field*. Tech. rep. Virginia Tech, 2004.

[7] NASA. *Spacecraft Magnetic Torques*. Tech. rep. NASA, 1969.

[8] Prof. Bernelli Franco. *Lecture notes in Attitude Dynamics and Control*. 2022.